Crystal structure of the M_5 muscarinic acetylcholine receptor

Ziva Vuckovic[1]*, Patrick R. Gentry[1]*, Alice E. Berizzi[1], Kunio Hirata[2], Swapna Varghese[3], Geoff Thompson[1], Emma T. van der Westhuizen[1], Wessel A.C. Burger[1], Raphaël Rahmani[3], Celine Valant[1], Christopher J. Langmead[1], Craig W. Lindsley[4], Jonathan Baell[3], Andrew B. Tobin[5], Patrick M. Sexton[1,6], Arthur Christopoulos[1¶] and David M. Thal[1¶]

1. Drug Discovery Biology and Department of Pharmacology, Monash Institute of Pharmaceutical Sciences, Monash University, Parkville 3052, Victoria, Australia

2. RIKEN, SPring-8 Center, Hyogo, Japan

3. Medicinal Chemistry, Monash Institute of Pharmaceutical Sciences, Monash University, Parkville 3052, Victoria, Australia

4. Departments of Pharmacology & Chemistry, Vanderbilt Center for Neuroscience Drug Discovery, Vanderbilt University, Nashville, Tennessee 37232, United States.

5. Centre for Translational Pharmacology, Institute of Molecular, Cell and Systems Biology, College of Medical, Veterinary and Life Sciences, University of Glasgow, Glasgow G12 8QQ, United Kingdom.

6. School of Pharmacy, Fudan University, Shanghai 201203, China.

*These authors contributed equally to this work.
¶ To whom correspondence should be addressed:

David Thal, david.thal@monash.edu

Arthur Christopoulos, arthur.christopoulos@monash.edu

Abstract

The human M_5 muscarinic acetylcholine receptor (mAChR) has recently emerged as an exciting therapeutic target for treating a range of disorders, including drug addiction. However, a lack of structural information for this receptor subtype has limited further drug development and validation. Here we report a high-resolution crystal structure of the human M_5 mAChR bound to the clinically used inverse agonist, tiotropium. This structure allowed for a comparison across all five mAChR family members that revealed important differences in both orthosteric and allosteric sites that could inform the rational design of selective ligands. These structural studies together with chimeric swaps between the extracellular regions of the M_2 and M_5 mAChR further revealed the structural insight into "kinetic-selectivity", where ligands show differential residency times between related family members. Collectively, our study provides important insights into the nature of orthosteric and allosteric ligand interaction across the mAChR family that could be exploited for the design of selective ligands.

Significance Statement

The five subtypes of the muscarinic acetylcholine receptors (mAChRs) are expressed throughout the central and peripheral nervous system where they play a vital role in physiology and pathologies. Recently, the M_5 mAChR subtype has emerged as an exciting drug target for the treatment of drug addiction. We have determined the atomic structure of the M_5 mAChR bound to the clinically used inverse agonist tiotropium. The M_5 mAChR structure now allows for a full comparison of all five mAChR subtypes and reveals subtle differences in the extracellular loop (ECL) regions of the receptor that mediate orthosteric and allosteric ligand selectivity. Together these findings open the door for future structure-based design of selective drugs that target this therapeutically important class of receptors.

Introduction

The muscarinic acetylcholine (ACh) receptors (mAChRs) are Class A G protein-coupled receptors (GPCRs) that together with the nicotinic acetylcholine receptors facilitate the actions of the neurotransmitter, ACh, throughout the body. The mAChR family comprises five subtypes where M_1, M_3, and M_5 are preferentially coupled to the $G_{q/11}$ protein-mediated signalling pathways, and M_2 and M_4, show preference for $G_{i/o}$ protein-dependent signalling. Localization studies have revealed that the mAChR subtypes are differentially distributed, with M_1, M_4, and M_5 mAChRs found predominantly in the central nervous system (CNS), where they are essential for normal neuronal function, while M_2 and M_3 mAChRs are expressed more widely, including in the periphery, where they are involved in cardiovascular as well as gut motility and secretory processes (1).

Given the involvement of mAChRs in such a wide range of fundamental physiological processes, they have long been valued as targets for novel therapeutics, in particular the central M_1 and M_4 mAChRs, which have garnered attention due to their involvement in cognition and memory (2). In contrast, relatively less is known about the M_5 mAChR subtype, which represents less than 2% of the total CNS mAChR population (3, 4). Despite its low level of expression, this receptor plays a vital role in the mesolimbic reward pathway due to its presence on dopaminergic neurons of the ventral tegmental area (VTA) (5-8). Additionally, there is a large population of non-neuronal M_5 mAChRs located within the endothelium of the cerebral vasculature, suggesting that the receptor may modulate cerebral vasodilatory processes (9, 10). These observations correlate well with phenotypic data from M_5 mAChR knockout mice where the cerebral vasculature is constitutively constricted, resulting in decreased cerebral blood flow (11, 12). Additionally, M_5 mAChR knockout mice exhibited attenuated reward-seeking behaviour to drugs of addiction, such as cocaine and morphine in self-administration and conditioned place-preference experiments (13-15). Moreover, in recent studies involving rats (16-18), ethanol-seeking behaviour and oxycodone self-administration were attenuated by the selective M_5 mAChR negative allosteric modulator (NAM) ML375 (19). From these studies, the M_5 mAChR has emerged as a potential target for the treatment of drug addiction.

Despite such promising data, further study of the M_5 mAChR has been hindered by a lack of selective small molecule tool compounds. Designing conventional small molecule ligands that target the orthosteric ACh binding site of individual mAChR subtypes has been challenging due to the highly conserved sequence homology of the mAChR orthosteric site residues (1),

and in part due to a lack of detailed structural information for all five receptor subtypes. While structures of the M_1–M_4 mAChRs have been previously determined, there are no available structures for the M_5 mAChR. Therefore, to provide a complete structural comparison of all five family members and to gain insight into ligand binding we determined a high-resolution crystal structure of the M_5 mAChR.

Results

Crystallization and determination of the M_5 mAChR structure.

To determine the M_5 mAChR structure we designed a construct where residues 225-430 of intracellular loop 3 were removed and replaced with a T4 lysozyme (T4L) fusion protein. Additionally, to promote crystallization, the first 20 N-terminal amino acids were cleaved by a Tobacco Etch Virus (TEV) protease site engineered into the receptor (Supplementary Figure 1a). The inverse agonist, tiotropium, was used to stabilize the inactive state as it has a slow dissociation rate at the M_5 mAChR (20), and was also used in the determination of the M_1, M_3, and M_4 mAChR structures (21, 22). The M_5-T4L•tiotropium complex was crystallized in lipidic cubic phase (LCP), and crystals were obtained within 1-2 days; however, despite many rounds of optimization, diffraction was limited to 7 Å. To improve the resolution we built upon a study from Yasuda *et al.* (23) that predicted that mutation of the amino acid at position 3.39 (numbered according to Ballesteros-Weinstein (24)) to Arg would create a thermostabilized receptor by promoting an ionic bond between this residue and the highly conserved $D^{2.50}$ residue. Recently, the same $S^{3.39}R$ mutation was applied to the M_2 mAChR resulting in a series of higher resolution structures (25). Although introduction of the $S117^{3.39}R$ mutation resulted in a construct that binds the antagonists NMS or tiotropium with a slightly reduced affinity relative to the WT M_5 mAChR, the effect of the mutation on reducing ACh affinity was substantially more pronounced (Supplementary Figure 1b-e), consistent with the ability of the construct to favour an inactive over an active state. Similar differential effects on antagonist versus agonist affinity were previously observed for $S^{3.39}R$ at the M_2 mAChR (25). Notably, introduction of the $S117^{3.39}R$ mutation increased our M_5 mAChR yields during purification and resulted in crystals that diffracted to a resolution of 3.4 Å. Data were collected from approximately 130 crystals, and the structure was determined by molecular replacement using the M_3 structure (PDB: 4U15) and an ensemble of T4L structures as templates (Figure 1a, Supplementary Table 1).

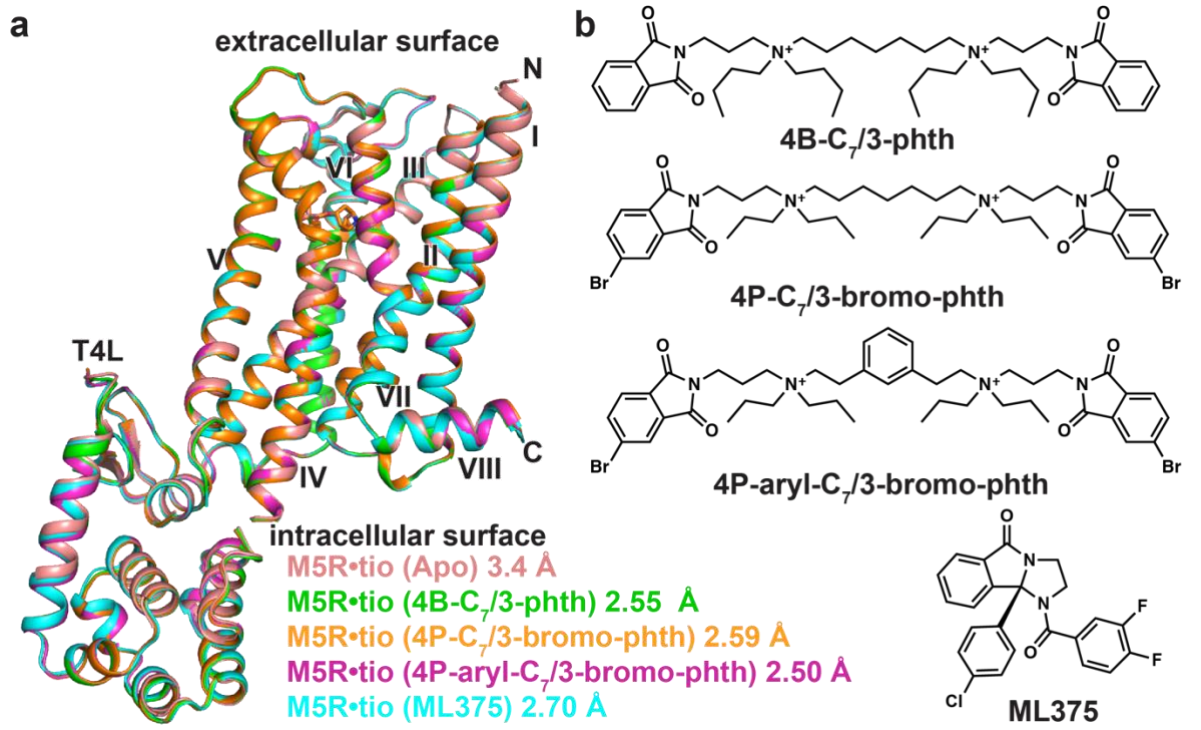

Figure 1. Structures of M_5-T4L bound to tiotropium. (a) Overlay of five different M_5 mAChR structures determined in the presence of tiotropium and **(b)** different allosteric modulators. The structure from 4B-C_7/3-phth was the most resolved of all the datasets and is used in all further comparisons (Supplementary Table 1).

To investigate the nature of NAMs binding to the M_5 mAChR, we attempted to obtain co-crystal structures. Given that the bis-ammonium alkane type ligands tend to have higher affinities for the M_5 mAChR than the prototypical modulator, gallamine (26), we tried to obtain a ternary complex structure of the M_5 mAChR with tiotropium and several bis-ammonium alkane ligands (Figure 1b). We initially used the modulator, 4B-C_7/3-phth, which resulted in crystals that grew to a much larger size and diffracted to a resolution of 2.55 Å (Figure 1, Supplementary Table 1, Supplementary Figure 2). Based on previous data (27), we predicted that 4B-C_7/3-phth would bind in the extracellular vestibule (ECV). While there were regions of strong electron density present in the ECV, we could not unambiguously model 4B-C_7/3-phth into the density as a molecule of the precipitant, polyethylene glycol 400 (PEG400), also likely binds in this site (22, 28), and may explain why researchers have had difficulty in obtaining co-NAM bound structures for the mAChRs.

Subsequently, we designed two new bis-ammonium alkane analogs using the higher affinity 4P-C_7/3-phth scaffold (27) to try and improve modulator affinity (Figure 1b, Supplementary

Figure 3a, Supplementary Table 2) and detectability by X-rays. The first modification added two bromine atoms (4P-C_7/3-bromo-phth) to increase the size of the pthalamide groups (29), and the second modification rigidified the flexible 7-carbon linker with an aromatic hydrocarbon (4P-aryl-C_7/3-bromo-phth). Both ligands displayed an increased affinity for the M_5 mAChR versus 4B-C_7/3-phth, but had a slightly reduced affinity in relation to the parent compound (4P-C_7/3-phth) when assayed for NAM activity in inhibiting [^{3}H]NMS radioligand binding (Supplementary Figure 3a, Supplementary Table 2). Like 4B-C_7/3-phth, the addition of either 4P-C_7/3-bromo-phth or 4P-aryl-C_7/3-bromo-phth to purified M_5 mAChR and reconstitution into LCP yielded crystals that diffracted to a higher resolution (Supplementary Table 1). A full data set for 4P-aryl-C_7/3-bromo-phth was collected at wavelength of 0.92 Å to maximize the anomalous Br signal in a single wavelength anomalous diffraction experiment, however, no such signal was detected, suggesting that 4P-aryl-C_7/3-bromo-phth was not present in the structure. Since the structure was solved by merging a large number of datasets, there is possibility that the Br signal for the NAM would be averaged out if NAM occupancy is low. However, inspection of different datasets did not indicate that this was the case.

As an alternate strategy, we attempted to determine a co-crystal structure with the structurally diverse M_5 mAChR selective NAM, ML375 (19). In comparison to the bis-ammonium ligands, the addition of ML375 resulted in a slightly lower resolution structure (2.7 Å, Supplementary Table 1) and, as was the case with the bis-ammonium NAMs, we were not able to assign ML375 into any electron density. Comparison of all M_5 mAChR structures showed that they were nearly identical, with root mean square deviation values of 0.09–0.22 Å. The higher resolution 2.55 Å M_5•tiotropium (4B-C_7/3-phth) structure was used for further comparison, as this was the best resolved and modelled structure.

Family-wide comparison of all mAChR subtypes.

The solution of the M_5 mAChR structure allows the first complete subtype-wide comparison of this important GPCR family. The structure of the M_5 mAChR is similar to the previously determined structures of the M_1-M_4 mAChR subtypes (21, 22, 30) with a root mean squared deviation of 0.5-0.8 Å (Figure 2a) for the seven-transmembrane domain across all subtypes. The five mAChR subtypes are most similar in the orthosteric binding site, which is the most conserved region of the receptor. The fact that our M_5 mAChR structure was obtained in complex with the same ligand (tiotropium), as the M_1, M_3 and M_4 mAChR structures, allowed for specific, detailed comparison of residues lining this orthosteric binding site (Figures 2b,c).

This comparison demonstrated that the residues within the orthosteric pocket are absolutely conserved between the receptors. Although there is no tiotropium bound M_2 mAChR structure, there are now six different inactive state M_2 mAChR structures, which include structures bound with the non-selective ligands QNB and NMS, and the M_2 mAChR selective ligand, AF-DX384 (25). The 2.3 Å M_2•NMS structure is most similar to the tiotropium bound mAChR structures, though residues $Y^{3.33}$ and $Y^{7.39}$ of the "tyrosine lid" ($Y^{3.33}$, $Y^{6.51}$, and $Y^{7.39}$) are positioned in a distinct conformation in comparison to the tiotropium bound structures. These differences in the tyrosine lid positions are more pronounced in the M_2•AF-DX384 structures, allowing the accommodation of this bulkier ligand into the orthosteric binding pocket (Figures 2b-c).

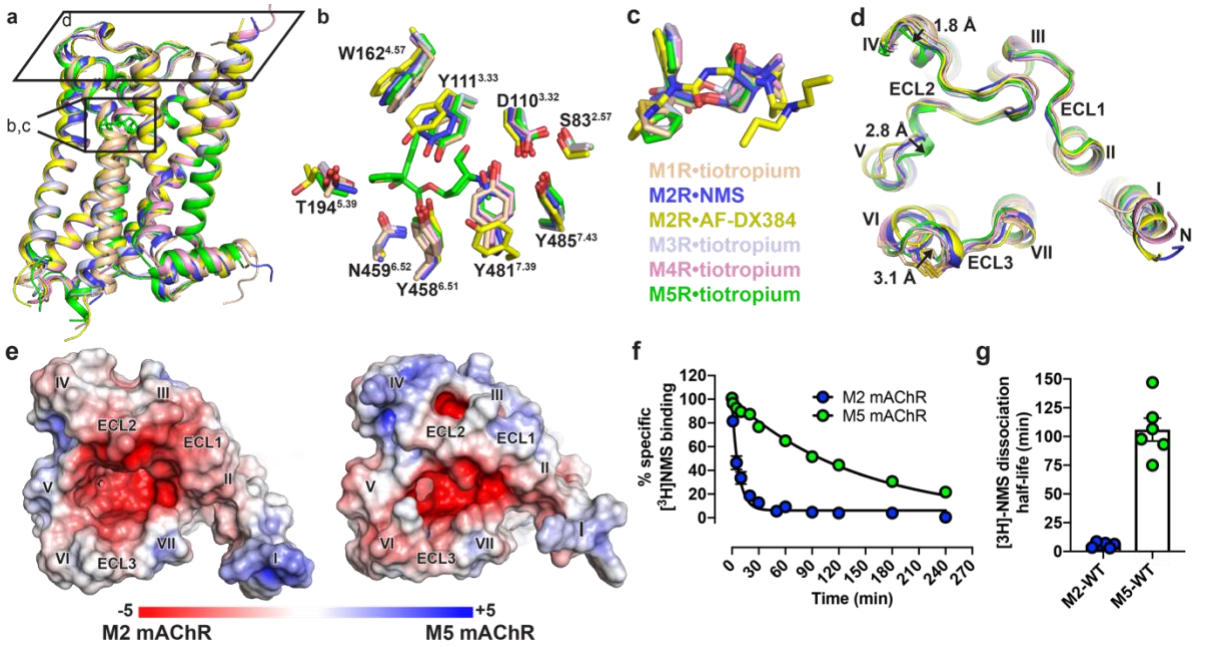

Figure 2. Structural comparison of M_1-M_5 mAChRs. (a) The overall view of the M_1-M_5 mAChR structures aligned to the M_5 mAChR and shown as cartoons. M_1•tiotropium is coloured peach (PDB: 5CXV), M_2•NMS dark blue (5ZKC), M_2•AF-DX384 yellow (5ZKB), M_3•tiotropium light blue (4U15), M_4•tiotropium pink (5DSG) and M_5•tiotropium green (6OL9). **(b)** Comparison of residues (stick representation) lining the orthosteric site with tiotropium from the M_5 mAChR displayed, and **(c)** overlay of the orthosteric ligands. **(d)** View from the extracellular surface comparing differences in the ECL regions across the M_1-M_5 mAChRs. Distances between the backbone of M_1 and M_5 mAChR residues in ECL2 and ECL3 are shown and indicated by arrows. **(e)** Electrostatic and surface potential of M_2 and M_5 mAChR (+5kT/e in blue and -5kT/e in red) mapped on the surface of the receptors calculated

at pH 7.0 using PDB2PQR and APBS (31). **(f)** Comparison of dissociation rate and **(g)** dissociation half-life of [^{3}H]NMS by the addition of 10 μM atropine at the M_2 and M_5 mAChRs.

Subtle yet notable differences between the mAChR subtypes are observed for ECL2 and ECL3, corresponding to regions that are the least conserved across the receptors (Figure 2d). At ECL2 there is a 1.8 Å difference across all five subtypes beginning at the first non-conserved residue of ECL2. As ECL2 progresses towards TM5, a conserved 3_{10} helix motif moves inward by 2.8 Å in the M_5 mAChR when compared to the M_1 structure. Similarly, the conserved ECL3 disulphide bond is displaced inwards by 3.1 Å for the M_3 and M_5 mAChRs (Figure 2d), relative to the other subtypes. These observed differences in the positons of ECL2 and ECL3, along with differences in amino acid composition contribute to a more constricted entrance to the orthosteric binding site at the M_5 (and M_3) versus the M_2 mAChR (Figure 2e). Furthermore, this contraction of the entrance in the antagonist-bound structures may contribute to the slower dissociation rate of orthosteric ligands from the M_5 and M_3 mAChRs, in comparison to other subtypes like the M_2 mAChR. For example, despite having similar equilibrium binding affinities, [^{3}H]NMS dissociates 18-fold more slowly at the M_5 than the M_2 mAChR with half-lives of dissociation of 100 ± 11.6 and 5.6 ± 1.2 min, respectively (Figure 2f,g).

Structural differences between the extracellular vestibules (ECVs) of the M_2 and M_5 mAChRs.

An alternative strategy to generating selective ligands is to target non-conserved allosteric sites (32). This has been extensively explored for the mAChR family where a palette of both positive and negative allosteric modulators has been identified (33, 34). Structural and mutagenesis studies have established that many of these ligands bind to a "common" allosteric site that is located above the orthosteric site and within an ECV (Figure 3, Supplementary Figure 4) (35). In fact, the M_5 mAChR has often served as model system for early research into understanding the binding mode and mechanism of selectivity for prototypical modulators, such as the bis-ammonium alkane ligands (Figure 1b), that have higher sensitivity for modulating the M_2 mAChR and lower sensitivity for the M_5 mAChR (26, 36-39). These studies identified non-conserved residues in ECL2 ($P179^{-4}$, $E182^{-1}$, and $Q184^{+1}$; superscript indicates the position of ECL2 residues relative to the conserved Cys in ECL2) and TM7 ($V474^{7.32}$ and $H484^{7.36}$) as residues that can account for M_2/M_5 subtype selectivity. Comparison of the ECV between the

M_2 and M_5 mAChRs confirm differences in the orientations and positions of these residues that could mediate the selectivity. Namely, $P179^{-4}$ in ECL2 restricts the position of $E182^{-1}$ forcing the residue into the ECV near $Q184^{+1}$. Residue $Q184^{+1}$, which is a F/Y residue for the M_1-M_4 mAChRs subtypes, is a key residue for the activity of many allosteric modulators. Other major differences between the M_2/M_5 ECVs are in the positions of non-conserved residues lining the top of TM6 starting from $S465^{6.58}$ across ECL3 and down to residue $H478^{7.36}$ in TM7. At the M_5 mAChR these residues are bulkier and point more inward constricting the overall size of the ECV (Figure 3).

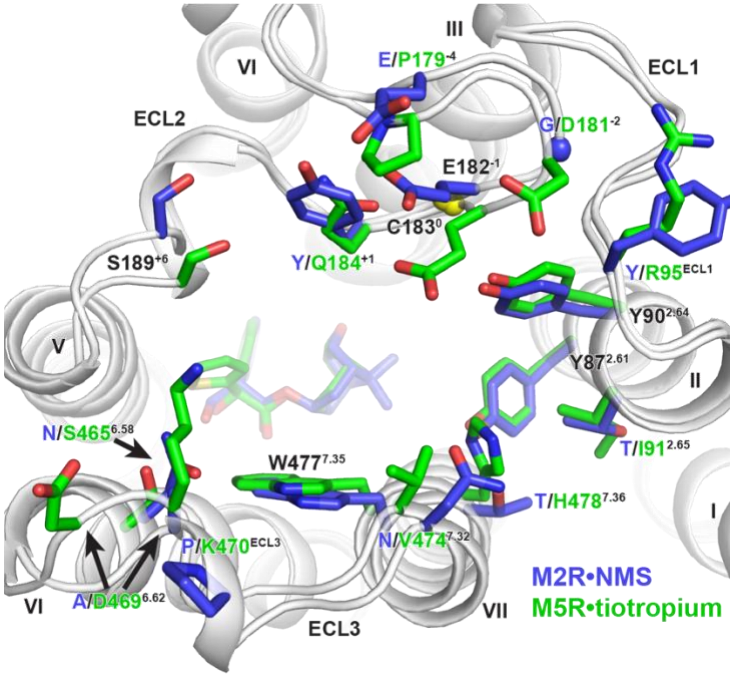

Figure 3. Comparison of residues lining the extracellular vestibule of the M_2 and M_5 mAChR. M_2•NMS is shown in dark blue and M_5•tiotropium in green. Conserved residues are labelled black and non-conserved residues are coloured according to receptor subtype. Residues are numbered based on the M_5 mAChR, with residues in ECL2 numbered relative to the conserved cysteine in ECL2, which is shown as a yellow sphere.

Role of the M_5 and M_2 mAChR ECL regions in orthosteric and allosteric ligand binding. The effect of ECL regions on orthosteric ligand access and egress has significant biological and clinical relevance (40). Therefore, to investigate the role of the ECLs on modulating the slower dissociation kinetics of the M_5 mAChR in comparison to the M_2 mAChR, we designed full ECL1, ECL2, and/or ECL3 chimeric swaps between the two subtypes (Figure 4). The ECL chimeras had similar levels of expression and binding of [^{3}H]NMS to wild type receptors

(Supplementary Table 3). As previously noted, the M_2 mAChR has a shorter half-life for [^{3}H]NMS dissociation in comparison to the M_5 mAChR (Figure 2f). Incorporation of the M_2 ECL1 or ECL3 into the M_5 mAChR increased [^{3}H]NMS dissociation, while the reciprocal chimeric swap decreased [^{3}H]NMS dissociation at the M_2 mAChR. Unexpectedly, it was the ECL1 swaps that had the largest effect on [^{3}H]NMS dissociation between the two subtypes, particularly at the M_5 mAChR (Figure 4, Supplementary Table 4). A possible structural explanation for this observation could be that R95^{ECL1}, which is a conserved Tyr residue at the M_1-M_4 subtypes, is capable of forming an ionic bond with either the M_5 ECL2 residue, D181^{-2}, or in the case of the M_2 ECL1 chimera residue D173^{-3} (Figure 3, Supplementary Figure 4). Such an interaction could tether ECL1 and ECL2 limiting their overall dynamics and thus reduce rates of orthosteric ligand dissociation. It is important to note that R95^{ECL1} is involved in an ionic interaction mediated through the crystal lattice with a neighbouring T4L molecule (Supplementary Figure 2d-f), and as a result it does not directly interact with D181^{-2} in the M_5 mAChR structure though it is well positioned to do so.

A hallmark feature of an allosteric ligand that modulates orthosteric ligand affinity is the ability to either increase or decrease the rate of dissociation of an orthosteric ligand. To examine the effect of allosteric modulators on NMS dissociation across the M_5 and M_2 ECL chimeras, we used the bis-ammonium alkane ligand 4P-C_7/3-phth, which had been previously studied at the M_2 mAChR and had high affinity for the M_5 mAChR (Supplementary Table 2), or the M_5 selective modulator ML375 (19, 27). In the presence of ML375, [^{3}H]NMS dissociation was reduced at the M_5 mAChR and had no effect at the M_2 mAChR, whereas the addition of 4P-C_7/3-phth reduced radioligand dissociation at the M_2 mAChR but not at the M_5 mAChR (Figure 4, Supplementary Table 4). The ECL1 and ECL3 chimeric swaps had little effect on the activity of ML375 for either receptor subtype, and slightly increased the activity of 4P-C_7/3-phth at the M_5 mAChR. For the ECL2 chimeras, there was no effect on activity of ML375. However, there was a loss of 4P-C_7/3-phth activity at the M_2 mAChR and a corresponding gain of activity at the M_5 mAChR. These results are in line with previous studies and highlight the importance of residues in ECL2, particularly M_2-Y177 and M_5-E184, on modulating the activity of bis-ammonium alkane ligands. Interestingly, when all three ECLs were swapped, the resulting M_2 and M_5 chimeric constructs functioned more like their swapped receptor counterpart. That is, for the M_2–M_5-all-ECL construct, 4P-C_7/3-phth had little effect, and although ML375 did not retard [^{3}H]NMS dissociation, it slightly increased the rate of [^{3}H]NMS dissociation suggesting an allosteric mode of action (Figure 4, Supplementary Table 4). Conversely, for the M_5–M_2-

all-ECL construct, 4P-C$_7$/3-phth retarded radioligand dissociation and, surprisingly, ML375 had no effect. While none of the chimeric constructs ever fully switched the basal dissociation rate of [^{3}H]NMS or ML375 activity to that observed for the corresponding WT constructs, the data nonetheless suggest that the ECL regions modulate the overall conformation of mAChRs and directly influence the dissociation of ligands from the orthosteric site.

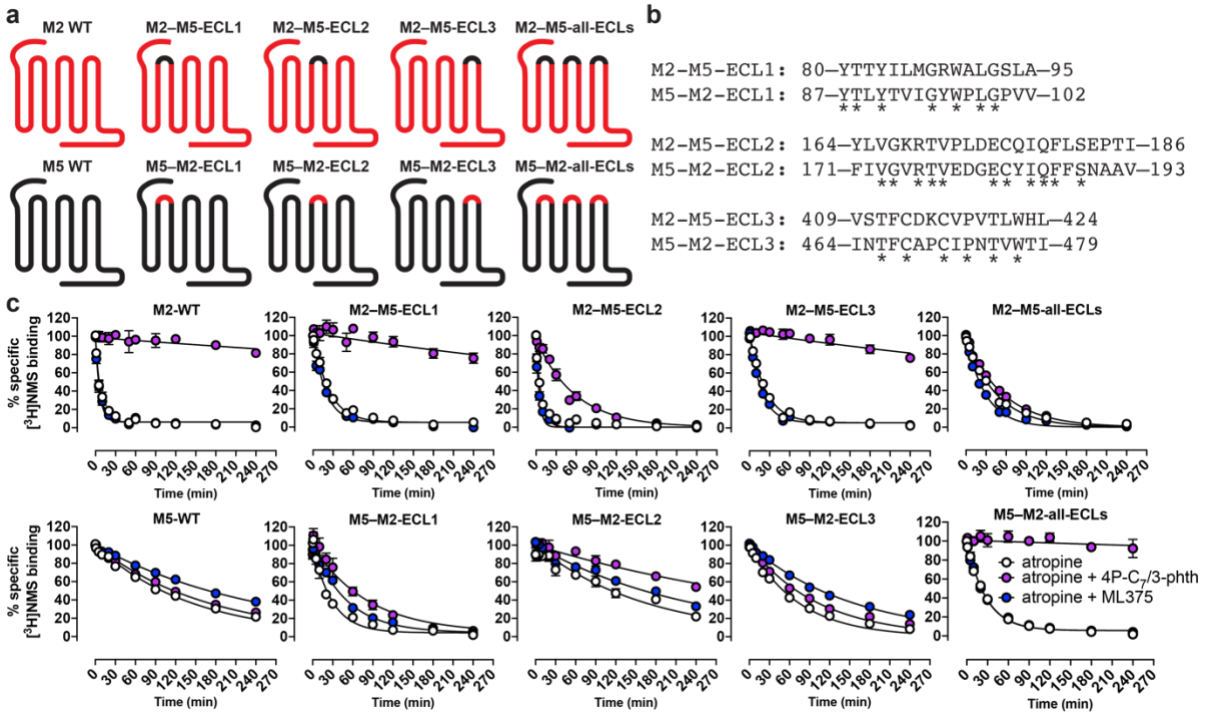

Figure 4. [^{3}H]NMS binding dissociation kinetic studies of chimeric swaps between the ECLs of the M$_2$ and M$_5$ mAChRs. (a) Cartoons and **(b)** amino acid sequence composition for the M$_2$ and M$_5$ ECL chimeras used in this study, with conserved residues noted by an asterix. **(c)** [^{3}H]NMS re-association was prevented by the addition of 10 µM atropine, and radioligand dissociation was monitored in the absence or presence of 10 µM ML375 or 10 µM 4P-C$_7$/3-phth. Data points represent the mean ± S.E.M. of three or more independent experiments performed in duplicate. Quantitative parameters derived from this experiment are listed in Supplementary Table 4.

Discussion

Individual mAChR subtypes have long been pursued as drug targets for a range of CNS disorders, and recent studies have begun to validate the M$_5$ mAChR as a novel target for the treatment of drug addiction (4, 41). In this study, we have determined a high-resolution crystal structure of the M$_5$ mAChR, thus allowing the first subtype-wide comparison for any aminergic

GPCR subfamily. Introduction of the inactive state stabilizing mutation S117$^{3.39}$R, which was recently used to stabilize the M_2 mAChR (25), was crucial to obtaining well-diffracting crystals and suggests that this mutation could be applied to aid the determination of inactive state structures for other related GPCRs. We further improved the resolution of the M_5 mAChR structure by adding allosteric modulators to the purified protein prior to crystallization. Despite the consistent increase in resolution that each of the allosteric modulator provided, we were not able to model any of the modulators into electron density. From a pharmacological perspective, a lack of modulator binding is not surprising, as all of the modulators tested in this study showed strong negative cooperativity with tiotropium (Supplementary Figure 3b). Nevertheless, it is still paradoxical that the addition of an allosteric modulator can clearly improve receptor crystallization and diffraction, though not be visible in any resulting structures. This phenomenon has been noted at other GPCRs, such as the M_2 mAChR that was crystallized in the presence of the modulator, alcuronium, and the CC chemokine receptor 2A that was crystallized in the presence of the modulator, AZD-6942, but where neither modulator could be observed in the resulting structures (25, 42).

Comparison of all five mAChR structures further confirms the well conserved transmembrane core and orthosteric binding site that has made the discovery of highly selective drugs for these receptor subtypes incredibly challenging. The most apparent structural differences between the mAChR subtypes is in the ECL regions. Though these differences are generally quite subtle they are important because they open up the possibility for designing selective molecules in a way that has not previously been possible (Supplementary Figure 4). For example, a recent crystal structure of the M_2 mAChR bound to the M_2-selective antagonist AF-DX384 revealed that selectivity is mediated by differential interactions between the ligand and residues in ECL2, which lead to an outward displacement in ECL2 and the top of TM5 (Figure 2d) (25). Likewise, by utilizing knowledge of a single amino acid difference in ECL2 between the M_2 and M_3 mAChRs, molecular docking and structure-based design led to the discovery of a new M_3-selective antagonist with 100-fold selectivity over the M_2 mAChR (43). These results are similar to the structure-based design of biased ligands targeting the D2 dopamine receptor that were designed by utilizing specific amino acid-ligand contacts in ECL2 and TM5 (44). Taken together, these findings indicate that the differential targeting of ECL residues may be a path forward for creating selective mAChR ligands. This is well supported by the fact that many mAChR-selective allosteric modulators interact with the ECL regions (27, 35), and suggest

that designing orthosteric ligands linked to allosteric pharmacophores, known as bitopic ligands, is a potential strategy for future structure-based drug design.

Drug discovery has typically focused on optimizing ligand affinity and selectivity. However, it is now apparent that binding kinetics are just as important (40, 45-47). This is illustrated two ways with the drug tiotropium as a pertinent example. First, tiotropium has slow rate of dissociation from the M_3 mAChR, which is a key feature of the drug that allows for a once daily dosing for the treatment of chronic obstructive pulmonary disease (48). Second, though tiotropium has the same equilibrium binding affinity for the M_3 and M_2 mAChRs, it exhibits kinetic selectivity for the M_3 over M_2 mAChR, by having substantially different rates of dissociation. This kinetic selectivity over the M_2 mAChR is postulated to be due to differences in the electrostatics and dynamics of the ECL region (48). The M_5 mAChR is similar to the M_3 mAChR with respect to having slow rates of orthosteric ligand dissociation (20), and data from our M_2/M_5 ECL chimeras support the idea of the ECL regions mediating kinetic selectivity as [^{3}H]NMS dissociation was switched between the M_2 and M_5 mAChRs (Figure 4). Notably, none of the combined ECL chimeras could ever fully switch the dissociation kinetics between subtypes, suggesting that other mechanisms are operative such as the global conformation of the ECLs. Our results also highlight the importance of the ECL regions on conferring sensitivity to allosteric modulators across different subtypes. By swapping out the entire ECL region between the M_2 and M_5 mAChRs we were able to completely alter the sensitivity of a modulator that is selective for the M_2 versus the M_5 mAChR and vice versa. These results support the importance of the ECL region for mediating ligand selectivity.

In summary, our reported M_5 mAChR crystal structure has allowed for the comparison of all five mAChR subtypes and has revealed that subtle differences in the ECL regions are a major determinant in ligand selectivity, regardless of the ligand being orthosteric or allosteric. As the M_1, M_4, and M_5 mAChRs continue to emerge as exciting drug targets for the treatment of CNS disorders, it will be important to understand both the structural and dynamic differences between all five mAChR subtypes in order to aid design of safer and more effective small-molecule therapeutics.

METHODS

Cloning. The human M_5 muscarinic receptor gene (cDNA.org) was cloned into a pFastBac vector containing an N-terminal Flag epitope and a C-terminal 10x histidine tag (cDNA.org). TEV cleavage site was introduced in order to remove the Flag epitope and the first 20 amino acids of the protein. Residues 225-430 of ICL3 were removed and replaced with T4L (Supplementary Figure 1). In addition, to stabilize the inactive state we introduced the mutation $S117^{3.39}R$ (23, 25). For pharmacology experiments M_2 and M_5 mAChR DNA was cloned into a pEF5/FTR/V5 vector (Invitrogen) using the Flp-In-CHO cell system (Invitrogen). To generate the M_2/M_5 ECL chimeras overlap extension PCR was used with primers specific to each ECL region. All DNA constructs were sequenced to confirm the correct nucleotide sequence using the Australian Genome Research Facility (Melbourne, Australia).

Synthesis of the bis-ammonium alkane ligands. 4B-C_7/3-phth and 4P-C_7/3-phth were synthesized as previously described (27). Synthesis for 4P-C_7/3-bromo-phth and 4P-aryl C_7/3-bromo-phth is described in Supplementary Data.

M5 receptor expression and purification. M_5-T4L was expressed in Sf9 cells using the Bac-to-Bac Baculovirus Expression System (Invitrogen). Cells were infected at a cell density of 4.0 x 10^6 cells/millilitre with 10 μM atropine. Cells were harvested 60-72 hours later. All purification steps were performed in the presence of 1 μM triotropium. Insect cells were lysed in a buffer containing 10 mM Tris pH 7.5, 1 mM EDTA, 1 mM $MgCl_2$, 1 mg/ml iodoacetamide, benzonase, and protease inhibitors. Cell membranes were then solubilised in 30 mM HEPES pH 7.4, 750 mM NaCl, 30 % glycerol, 1 % dodecyl maltoside (DDM), 0.2 % cholate, 0.03 % cholesterol hemisuccinate (CHS), 1 mM $MgCl_2$, 1 mg/ml iodoacetamide, benzonase and protease inhibitors for 90 minutes at 4°C. After removing the insoluble debris, 25 mL of Ni-NTA resin, 1 mg/ml iodoacetamide and protease inhibitors were added and incubated with the protein for 2 hours 4°C. The Ni-NTA resin was pelleted using a table top centrifuge and then washed using 30 mM HEPES pH 7.4, 750 mM NaCl, 30 % glycerol, 5 mM imidazole pH 8.0, 0.1 % DDM, 0.02 % cholate and 0.003 % CHS. The protein was eluted using the same buffer supplemented with 250 mM imidazole. The elution was supplemented with 2 mM $CaCl_2$ and then loaded onto an anti-Flag M1 antibody column. The buffer/DDM was exchanged into 30 mM HEPES pH 7.4, 100 mM NaCl, 2 mM $CaCl_2$, 0.1 % lauryl maltose neopentyl glycol (LMNG) and 0.01 % CHS over the course of 30 min. The resin was then washed with 10x CMC buffer (30 mM HEPES pH 7.4, 100 mM NaCl, 0.01 % LMNG and 0.001 % CHS) with

2 mM $CaCl_2$ before the protein was eluted using the same buffer supplemented with 10 mM EDTA and 0.2 mg/ml FLAG peptide. TEV protease was added (1mg) overnight at 4^{o}C before concentrating the protein for size-exclusion chromatography using a Superdex S200 increase column in 10x CMC buffer. Monodispersed fractions were pooled together (Supplementary Figure 2), concentrated to 80 absorbance units (~50 mg/ml) and flash frozen in small aliquots using liquid nitrogen.

Crystallization and structure determination. Purified M_5-T4L(S3.39R) bound to tiotropium was crystallized using LCP. For allosteric modulator co-crystallization, the modulator was added to purified protein at a final concentration of 2.5 mM. The sample was incubated on ice for 3 hours before it was mixed into 10:1 (w/w) monoolein:cholesterol in 1:1.5 w/w protein:lipid ratio. LCP crystallization was performed by spotting 25-30 nL of samples on siliconized 96-well glass plate overlaying the samples with 600 nL of precipitant solution using the Gryphon LCP (Art Robbins Instruments). Sealed glass plates were incubated at 20 ^{o}C. Crystals appeared in the first 24 hours and grew to full size in the following 1-2 days. The best diffracting crystals grew in 100 mM DL-Malic acid pH 6.0, 220-280 mM ammonium tartrate dibasic and 37-41% PEG 400. For the data collection, whole drops were harvested using mesh grid loops (Mitegen) and flash frozen in liquid nitrogen.

X-ray diffraction data were collected at the SPring-8 (Japan) beamline BL32XU (49) and the MX2 beamline at the Australian Synchrotron (50). Diffraction data at SPring-8 was collected using the automatic data-collection system ZOO (51). Diffraction data was processed using KAMO (52) with XDS (53). The structure was solved using molecular replacement with M_3-mT4L (4U15) as a search model for the receptor and an ensemble of T4L molecules for T4L. Structure refinement was performed with Phenix (54), and the models were validated with MolProbity (55). Structure figures were prepared with PyMol.

Pharmacology of crystallization constructs. Sf9 cells expressing M_5-T4L (S117R) or WT M_5 mAChR were harvested after 60 hours. Sf9 cell membranes were prepared by homogenization and centrifugation. The final membrane pellet was resuspended in 20 mM HEPES pH 7.4 and 0.1 mM EDTA. Protein concentration was determined by absorbance at 280 nm and membranes were stored at -80 ^{o}C. Assays were conducted in UniFilter-96 GF/B plates (PerkinElmer) with 1 ug of membranes per well in a final volume of 300 µl binding buffer consisting of 20 mM HEPES, 100 mM NaCl, and 10 mM $MgCl_2$ at pH 7.4. Non-specific binding was defined in the presence of 1 µM atropine. Assays were stopped by vacuum

filtration and washed three times with ice-cold 0.9% sodium chloride. Plates were allowed to dry before 40 µL of Microscint-0 (PerkinElmer) was added to each well. Radioactivity was measured on a MicroBeta2 microplate counter. [^{3}H]NMS affinity (K_A) was determined in saturation binding experiments using 7 different concentrations of [^{3}H]NMS (0.03–30 nM). Equilibration was 1 hour at room temperature. Competition binding assays and allosteric modulator assays were performed by incubating membranes with a K_A concentration of [^{3}H]NMS and varying concentrations of compounds. The reactions were left at room temperature and harvested after 4 hours. Similar competition experiments with tiotropium were performed in the absence and presence of 30 µM of the allosteric modulators.

Mammalian cell culture. For stable expression, DNA constructs in pEF5/FTR/V5 (ThermoFisher) were transfected into the Flp-In-CHO cell line (ThermoFisher) as previously described (22). A suspected error with the M_2–M_5-ECL1 and M_5–M_2-all-ECL cell lines led us to resequencing all of the constructs and performing transient transfections for these constructs and also retesting all of the M_2 cell lines. Cells were maintained in DMEM containing 10% FBS, 16 mM HEPES pH 7.4, and 400 µg ml^{-1} hygromycin B. Mycoplasma testing was performed regularly on cell lines using the MycoAlertTM kit (Lonza); cell lines were mycoplasma-free before experiments were conducted.

Pharmacology of the M_2/M_5 mAChR chimeras. Flp-In-CHO cells either stably or transiently expressing the M_2/M_5 mAChR chimeras were seeded in 96-well Isoplates (PerkinElmer Life Sciences) at a concentration of 20,000 – 25,000 cells per well a day before the experiment was performed in a humidified atmosphere at 37ºC, 5% CO_2. The next day, cells were washed with assay buffer consisting of 110 mM NaCl, 5.4 mM KCl, 1.8 mM $CaCl_2$, 1 mM $MgSO_4$, 25 mM glucose, 50 mM HEPES, and 58 mM sucrose, pH 7.4. Saturation binding experiments were performed similar to above with assay volumes of 150 µL. Kinetic binding dissociation experiments were performed by incubating cells with 0.2 nM [^{3}H]NMS for 3 hours at room temperature before a reverse time-course was performed. Dissociation was initiated by atropine and treatments consisted of 10 µM atropine and either vehicle, 10 µM ML375, or 10 µM 4P-C_7/3-phth being added at the indicated time points. At the end of the time course, radioligand was removed by inverting the plate and followed by 3 washes with ice-cold 0.9% sodium chloride. Bound radioactivity was assessed by liquid scintillation using Optiphase Supermix (100 µL) and counting on a MicroBeta2 Plate Counter.

Data Analysis. Data were analysed using Prism 8.2 (GraphPad). Saturation binding curves were fitted to a one site binding curve accounting for total and non-specific binding. Competition binding curves were fitted to a one-site binding inhibition model. Allosteric titrations between [^{3}H]NMS and modulators were fit to an allosteric ternary complex model. Radioligand dissociation data were fitted to a mono-exponential decay function.

Author Contributions. Z.V., P.R.G., and D.M.T. performed cloning, protein expression, purification, crystallization, data collection, structure refinement, and radioligand binding experiments on the crystallization constructs. K.H. collected and processed data all the data from SPring-8. S.J. and J.B. designed and performed the synthesis of 4P-C_7/3-bromo-phth and 4P-aryl-C_7/3-bromo-phth. R.R. and J.B. designed and performed the synthesis of 4P-C_7/3-phth and 4B-C_7/3-phth. For the M_2/M_5 mAChR chimera experiments: Z.V. performed cloning and generated the stable cell lines. Molecular pharmacology experiments were performed by A.E.B., Z.V., E.T.W., G.T., and W.A.C.B. C.L. provided ML375. C.V., C.L., J.B., A.B.T., P.M.S., A.C., and D.M.T. provided overall project design and supervision. Z.V., P.R.G., A.C., and D.M.T. wrote the manuscript with contributions from all authors.

Acknowledgements. The synchrotron radiation experiments were performed at the BL32XU beamline at SPring-8 with the approval of JASRI (Proposal No. 2017B2731) and the MX2 beamline at the Australian Synchrotron (CAP13670). This work was funded by a Wellcome Trust Collaborative Award (201529/Z/16/Z), and supported by National Health and Medical Research Council of Australia (NHMRC) project (APP1138448) and program (APP1055134) grants. J.B. is a NHMRC Principal Research Fellow, P.M.S. and A.C. are NHMRC Senior Principal Research Fellows, and D.M.T. is an Australian Research Council Discovery Early Career Research Fellow.

Uncategorized References

1. M. P. Caulfield, N. J. Birdsall, International Union of Pharmacology. XVII. Classification of muscarinic acetylcholine receptors. *Pharmacol Rev* **50**, 279-290 (1998).

2. A. C. Kruse, J. Hu, B. K. Kobilka, J. Wess, Muscarinic acetylcholine receptor X-ray structures: potential implications for drug development. *Curr Opin Pharmacol* **16**, 24-30 (2014).

3. R. P. Yasuda *et al.*, Development of antisera selective for m4 and m5 muscarinic cholinergic receptors: distribution of m4 and m5 receptors in rat brain. *Mol Pharmacol* **43**, 149-157 (1993).

4. A. M. Bender, A. T. Garrison, C. W. Lindsley, The Muscarinic Acetylcholine Receptor M5: Therapeutic Implications and Allosteric Modulation. *ACS Chem Neurosci* **10**, 1025-1034 (2019).

5. G. L. Forster, C. D. Blaha, Laterodorsal tegmental stimulation elicits dopamine efflux in the rat nucleus accumbens by activation of acetylcholine and glutamate receptors in the ventral tegmental area. *Eur J Neurosci* **12**, 3596-3604 (2000).

6. G. L. Forster, C. D. Blaha, Pedunculopontine tegmental stimulation evokes striatal dopamine efflux by activation of acetylcholine and glutamate receptors in the midbrain and pons of the rat. *Eur J Neurosci* **17**, 751-762 (2003).

7. G. L. Forster, J. S. Yeomans, J. Takeuchi, C. D. Blaha, M5 muscarinic receptors are required for prolonged accumbal dopamine release after electrical stimulation of the pons in mice. *J Neurosci* **22**, RC190 (2002).

8. S. Steidl, A. D. Miller, C. D. Blaha, J. S. Yeomans, M(5) muscarinic receptors mediate striatal dopamine activation by ventral tegmental morphine and pedunculopontine stimulation in mice. *PLoS One* **6**, e27538 (2011).

9. A. Elhusseiny, Z. Cohen, A. Olivier, D. B. Stanimirovic, E. Hamel, Functional acetylcholine muscarinic receptor subtypes in human brain microcirculation: identification and cellular localization. *J Cereb Blood Flow Metab* **19**, 794-802 (1999).

10. S. K. Tayebati, M. A. Di Tullio, D. Tomassoni, F. Amenta, Localization of the m5 muscarinic cholinergic receptor in rat circle of Willis and pial arteries. *Neuroscience* **122**, 205-211 (2003).

11. R. Araya *et al.*, Loss of M5 muscarinic acetylcholine receptors leads to cerebrovascular and neuronal abnormalities and cognitive deficits in mice. *Neurobiol Dis* **24**, 334-344 (2006).

12. M. Yamada *et al.*, Cholinergic dilation of cerebral blood vessels is abolished in M(5) muscarinic acetylcholine receptor knockout mice. *Proc Natl Acad Sci U S A* **98**, 14096-14101 (2001).

13. A. S. Basile *et al.*, Deletion of the M5 muscarinic acetylcholine receptor attenuates morphine reinforcement and withdrawal but not morphine analgesia. *Proc Natl Acad Sci U S A* **99**, 11452-11457 (2002).
14. A. Fink-Jensen *et al.*, Role for M5 muscarinic acetylcholine receptors in cocaine addiction. *J Neurosci Res* **74**, 91-96 (2003).
15. M. Thomsen *et al.*, Reduced cocaine self-administration in muscarinic M5 acetylcholine receptor-deficient mice. *J Neurosci* **25**, 8141-8149 (2005).
16. A. E. Berizzi *et al.*, Muscarinic M5 receptors modulate ethanol seeking in rats. *Neuropsychopharmacology* **43**, 1510-1517 (2018).
17. R. W. Gould *et al.*, Acute Negative Allosteric Modulation of M5 Muscarinic Acetylcholine Receptors Inhibits Oxycodone Self-Administration and Cue-Induced Reactivity with No Effect on Antinociception. *ACS Chem Neurosci* 10.1021/acschemneuro.9b00274 (2019).
18. B. W. Gunter *et al.*, Selective inhibition of M5 muscarinic acetylcholine receptors attenuates cocaine self-administration in rats. *Addict Biol* **23**, 1106-1116 (2018).
19. P. R. Gentry *et al.*, Discovery of the first M5-selective and CNS penetrant negative allosteric modulator (NAM) of a muscarinic acetylcholine receptor: (S)-9b-(4-chlorophenyl)-1-(3,4-difluorobenzoyl)-2,3-dihydro-1H-imidazo[2,1-a]isoi ndol-5(9bH)-one (ML375). *J Med Chem* **56**, 9351-9355 (2013).
20. D. A. Sykes *et al.*, The Influence of receptor kinetics on the onset and duration of action and the therapeutic index of NVA237 and tiotropium. *J Pharmacol Exp Ther* **343**, 520-528 (2012).
21. A. C. Kruse *et al.*, Structure and dynamics of the M3 muscarinic acetylcholine receptor. *Nature* **482**, 552-556 (2012).
22. D. M. Thal *et al.*, Crystal structures of the M1 and M4 muscarinic acetylcholine receptors. *Nature* **531**, 335-340 (2016).
23. Y. Kajiwara, S. Yasuda, Y. Takamuku, T. Murata, M. Kinoshita, Identification of thermostabilizing mutations for a membrane protein whose three-dimensional structure is unknown. *J Comput Chem* **38**, 211-223 (2017).
24. J. A. Ballesteros, H. Weinstein, "[19] Integrated methods for the construction of three-dimensional models and computational probing of structure-function relations in G protein-coupled receptors" in Methods in Neurosciences, S. C. Sealfon, Ed. (Academic Press, 1995), vol. 25, pp. 366-428.

25. R. Suno *et al.*, Structural insights into the subtype-selective antagonist binding to the M2 muscarinic receptor. *Nat Chem Biol* **14**, 1150-1158 (2018).
26. X. P. Huang, S. Prilla, K. Mohr, J. Ellis, Critical amino acid residues of the common allosteric site on the M2 muscarinic acetylcholine receptor: more similarities than differences between the structurally divergent agents gallamine and bis(ammonio)alkane-type hexamethylene-bis-[dimethyl-(3-phthalimidopropyl)ammonium]dibromide. *Mol Pharmacol* **68**, 769-778 (2005).
27. R. O. Dror *et al.*, Structural basis for modulation of a G-protein-coupled receptor by allosteric drugs. *Nature* **503**, 295-299 (2013).
28. T. S. Thorsen, R. Matt, W. I. Weis, B. K. Kobilka, Modified T4 Lysozyme Fusion Proteins Facilitate G Protein-Coupled Receptor Crystallogenesis. *Structure* **22**, 1657-1664 (2014).
29. W. Bender, M. Staudt, C. Trankle, K. Mohr, U. Holzgrabe, Probing the size of a hydrophobic binding pocket within the allosteric site of muscarinic acetylcholine M2-receptors. *Life Sci* **66**, 1675-1682 (2000).
30. K. Haga *et al.*, Structure of the human M2 muscarinic acetylcholine receptor bound to an antagonist. *Nature* **482**, 547-551 (2012).
31. E. Jurrus *et al.*, Improvements to the APBS biomolecular solvation software suite. *Protein Sci* **27**, 112-128 (2018).
32. D. M. Thal, A. Glukhova, P. M. Sexton, A. Christopoulos, Structural insights into G-protein-coupled receptor allostery. *Nature* **559**, 45-53 (2018).
33. A. Bock, R. Schrage, K. Mohr, Allosteric modulators targeting CNS muscarinic receptors. *Neuropharmacology* **136**, 427-437 (2018).
34. K. J. Gregory, P. M. Sexton, A. Christopoulos, Allosteric modulation of muscarinic acetylcholine receptors. *Curr Neuropharmacol* **5**, 157-167 (2007).
35. W. A. C. Burger, P. M. Sexton, A. Christopoulos, D. M. Thal, Toward an understanding of the structural basis of allostery in muscarinic acetylcholine receptors. *J Gen Physiol* **150**, 1360-1372 (2018).
36. S. Buller, D. P. Zlotos, K. Mohr, J. Ellis, Allosteric site on muscarinic acetylcholine receptors: a single amino acid in transmembrane region 7 is critical to the subtype selectivities of caracurine V derivatives and alkane-bisammonium ligands. *Mol Pharmacol* **61**, 160-168 (2002).

37. A. L. Gnagey, M. Seidenberg, J. Ellis, Site-directed mutagenesis reveals two epitopes involved in the subtype selectivity of the allosteric interactions of gallamine at muscarinic acetylcholine receptors. *Mol Pharmacol* **56**, 1245-1253 (1999).

38. S. Prilla, J. Schrobang, J. Ellis, H. D. Holtje, K. Mohr, Allosteric interactions with muscarinic acetylcholine receptors: complex role of the conserved tryptophan M2422Trp in a critical cluster of amino acids for baseline affinity, subtype selectivity, and cooperativity. *Mol Pharmacol* **70**, 181-193 (2006).

39. U. Voigtlander *et al.*, Allosteric site on muscarinic acetylcholine receptors: identification of two amino acids in the muscarinic M2 receptor that account entirely for the M2/M5 subtype selectivities of some structurally diverse allosteric ligands in N-methylscopolamine-occupied receptors. *Mol Pharmacol* **64**, 21-31 (2003).

40. J. R. Lane, L. T. May, R. G. Parton, P. M. Sexton, A. Christopoulos, A kinetic view of GPCR allostery and biased agonism. *Nat Chem Biol* **13**, 929-937 (2017).

41. A. C. Kruse *et al.*, Muscarinic acetylcholine receptors: novel opportunities for drug development. *Nat Rev Drug Discov* **13**, 549-560 (2014).

42. A. K. Apel *et al.*, Crystal Structure of CC Chemokine Receptor 2A in Complex with an Orthosteric Antagonist Provides Insights for the Design of Selective Antagonists. *Structure* **27**, 427-438.e425 (2019).

43. H. Liu *et al.*, Structure-guided development of selective M3 muscarinic acetylcholine receptor antagonists. *Proc Natl Acad Sci U S A* **115**, 12046-12050 (2018).

44. J. D. McCorvy *et al.*, Structure-inspired design of beta-arrestin-biased ligands for aminergic GPCRs. *Nat Chem Biol* **14**, 126-134 (2018).

45. A. Strasser, H. J. Wittmann, R. Seifert, Binding Kinetics and Pathways of Ligands to GPCRs. *Trends Pharmacol Sci* **38**, 717-732 (2017).

46. D. C. Swinney, B. A. Haubrich, I. Van Liefde, G. Vauquelin, The Role of Binding Kinetics in GPCR Drug Discovery. *Curr Top Med Chem* **15**, 2504-2522 (2015).

47. R. A. Copeland, The drug-target residence time model: a 10-year retrospective. *Nat Rev Drug Discov* **15**, 87-95 (2016).

48. C. S. Tautermann *et al.*, Molecular basis for the long duration of action and kinetic selectivity of tiotropium for the muscarinic M3 receptor. *J Med Chem* **56**, 8746-8756 (2013).

49. K. Hirata *et al.*, Achievement of protein micro-crystallography at SPring-8 beamline BL32XU. *Journal of Physics: Conference Series* **425**, 012002 (2013).

50. D. Aragao *et al.*, MX2: a high-flux undulator microfocus beamline serving both the chemical and macromolecular crystallography communities at the Australian Synchrotron. *J Synchrotron Radiat* **25**, 885-891 (2018).
51. K. Hirata *et al.*, ZOO: an automatic data-collection system for high-throughput structure analysis in protein microcrystallography. *Acta Crystallogr D Struct Biol* **75**, 138-150 (2019).
52. K. Yamashita, K. Hirata, M. Yamamoto, KAMO: towards automated data processing for microcrystals. *Acta Crystallogr D Struct Biol* **74**, 441-449 (2018).
53. W. Kabsch, Xds. *Acta Crystallogr D Biol Crystallogr* **66**, 125-132 (2010).
54. P. D. Adams *et al.*, PHENIX: a comprehensive Python-based system for macromolecular structure solution. *Acta Crystallogr D Biol Crystallogr* **66**, 213-221 (2010).
55. V. B. Chen *et al.*, MolProbity: all-atom structure validation for macromolecular crystallography. *Acta Crystallogr D Biol Crystallogr* **66**, 12-21 (2010).